Journal of Marine Research, 75, 531–555, 2017

Observations of the East Madagascar Current system: Dynamics and volume transports

by Aksel Voldsund[1,2], Borja Aguiar-González[3,4], Tor Gammelsrød[1], Jens-Otto Krakstad[5], and Jenny Ullgren[6,7]

ABSTRACT

The South Equatorial Current (SEC) in the Indian Ocean bifurcates when it reaches Madagascar leading, respectively, to the North East Madagascar Current (NEMC), which contours the island flowing northwestward, and to the South East Madagascar Current (SEMC), which flows southwestward. Both branches eventually contribute to the greater Agulhas Current system and thus play a part in the global ocean circulation. In addition, these currents have important effects on the local conditions for marine life. In this study, the NEMC and the SEMC are investigated based on a comprehensive, multidisciplinary survey of the east coast of Madagascar in 2008. Results from conductivity-temperature-depth stations, underway measurements with thermosalinograph and fluorometer, and ship-mounted acoustic Doppler current profiler are discussed along with concomitant remotely sensed data. Maximum core velocities of >150 cm s^{-1} were observed in both the NEMC and the SEMC. The SEMC appeared as a nearshore southward jet, which extended at its widest nearly 200 km offshore. Near the southern tip of Madagascar, the SEMC was flanked by reverse velocities: a northeastward current about 30 km wide along the coast and a northeastward offshore current greater than 140 km wide suggesting the presence of the South Indian Ocean Countercurrent. The NEMC had the structure of a narrow nearshore jet, with weak currents beyond 100 km offshore. Volume transport for the upper 1,100 m was estimated to be 22 Sverdrup (Sv) for the SEMC and 48 Sv for the NEMC. The high NEMC transport compared with earlier estimates might be because of anomalously high influx of the SEC during the measurement period. Off the south coast, an undercurrent below 900 m carried an equatorward transport of 3.1 Sv. No undercurrent was observed in the north, but a geostrophic velocity minimum and a similar vertical velocity shear between surface and subsurface currents were found at the level where such a countercurrent has been previously observed from direct measurements.

Keywords: Indian Ocean, east Madagascar, western boundary current, volume transport, in situ observations, remote sensing

1. Geophysical Institute, University of Bergen, 5000 Bergen, Norway.
2. Current address: Norwegian Mapping Authority, Hydrographic Service, P.O. Box 60, 4001 Stavanger, Norway.
3. NIOZ Royal Netherlands Institute for Sea Research, Department of Ocean Systems Sciences and Utrecht University, P.O. Box 59, 1790 AB Den Burg, Texel, the Netherlands.
4. Corresponding author: ***e-mail: aguiar@nioz.nl***
5. Institute of Marine Research, P.O. Box 1870 Nordnes, 5817 Bergen, Norway.
6. Nansen Environmental and Remote Sensing Center, Thormøhlens gate 47, 5006 Bergen, Norway.
7. Runde Environmental Centre, Rundavegen 237, 6096 Runde, Norway.

1. Introduction

The South Equatorial Current (SEC) in the Indian Ocean is driven by the trade winds and hits the east Madagascar coast near 18° S with some seasonal variation (Sætre and Da Silva 1984; Lutjeharms et al. 2006; Chen et al. 2014; Aguiar-González et al. 2016). After bifurcation the SEC feeds the East Madagascar Current (EMC) system, consisting of a southern and a northern branch, namely the South East Madagascar Current (SEMC) and the North East Madagascar Current (NEMC), respectively (Swallow, Fieux, and Schott 1988).

The southern branch turns west south of Madagascar toward the African continent and breaks up into a regular series of symmetric counterrotating vortex pairs (Ridderinkhof et al. 2013). Most of them split and propagate into the Agulhas Current system. Additionally, Chapman et al. (2003) reported that Lagrangian floats at 800–900 m depth occasionally took a shortcut directly toward the South African coast, making the southern contribution even more efficient. In this regard, Siedler et al. (2009) estimated that about 50% of the SEMC transport continues toward the Agulhas Current, and thus joins the southbound volume transport through the Mozambique Channel of about 17 Sverdrup (Sv) near 30° S (see Harlander et al. 2009; Ridderinkhof et al. 2010; Ullgren et al. 2012, 2016; Halo et al. 2014). The circulation in the Mozambique Channel is dominated by large anticyclonic eddies moving southward (Lutjeharms et al. 2000; Ridderinkhof and de Ruijter 2003; van der Werf et al. 2010; Halo et al. 2014). Lutjeharms et al. (2012) showed that the volume transport near the Mozambican coast occasionally exceeds 80 Sv.

The NEMC turns west north of Madagascar as a strong jet with a strong positive vorticity. Backeberg and Reason (2010) argue, using remote-sensing data and a numerical model, that this may contribute to the formation of the Mozambique Channel eddies. Accordingly, both the SEMC and NEMC form important inputs to the Agulhas Current system. Downstream, the Agulhas Current leaks warm, saline water to the South Atlantic, which may influence the Atlantic meridional overturning circulation (Biastoch et al. 2009; Beal et al. 2011; Simon et al. 2015). Thus, the study of the EMC system is of particular interest as it is contributing to the global interbasin water exchange.

The east Madagascar boundary currents have been studied by Swallow, Fieux, and Schott (1988) using conductivity-temperature-depth (CTD) observations and by Schott et al. (1988) based on 11-month current meter moorings. These investigations concentrated on a transect at 23° S and one toward the northeast at the northern tip of Madagascar (12° S). The studies reported southward transports carried by the SEMC of about 20 Sv near 23° S, and northwestward transports carried by the NEMC of about 29 Sv at 12° S. Swallow, Fieux, and Schott (1988) also described a northward-bound surface countercurrent at about 100 km from shore in their transect at 23° S. This current was later named the South Indian Ocean Countercurrent (SICC) and was further studied by Siedler et al. (2006), Palastanga et al. (2007), Menezes et al. (2014), and, more recently, by Lambert, Le Bars, and de Ruijter (2016) and Menezes et al. (2016). During a research cruise with both ship-mounted and lowered acoustic Doppler current profiler (LADCP), Nauw et al. (2008) observed the SICC

and also discovered an equatorward current below the SEMC centered at about 1,000 m depth, which they named the East Madagascar Undercurrent (EMUC). In a recent study based on about 2.5 years of velocity observations along a full-depth mooring line at 23° S, Ponsoni et al. (2016) and Ponsoni, Aguiar-González, Maas, et al. (2015) obtained a mean poleward transport of 18.3 Sv for the SEMC and an equatorward transport of 1.3 Sv for the EMUC. Furthermore, using a CTD system equipped with LADCP, Ponsoni, Aguiar-González, Nauw, et al. (2015) reported for the first time an undercurrent also at 12° S, which they named the North Madagascar Undercurrent (NMUC). It was found to have a southeastward transport of about 3.5 Sv.

During the last decade, studies of the EMC system have been enriched by the use of satellite altimeter observations (Ducet, Le Traon, and Reverdin 2000) and an updated version of the World Ocean Database (Boyer et al. 2009), which includes data from the increasing number of profiling floats. For instance, Nauw et al. (2006) used the World Ocean Circulation Experiment (WOCE) hydrographic data and (pre-WOCE) data from the World Ocean Database to investigate the characteristics and formation of intrathermocline eddies southeast of Madagascar; Ponsoni et al. (2016) used satellite altimeter measurements to investigate the interannual variability of the EMC; and Chen et al. (2014) made use of monthly climatological temperature and salinity fields and altimeter data to investigate seasonal variations in the SEC bifurcation latitude, upstream of the EMC system.

The present work is based on a detailed survey with R/V *Dr. Fridtjof Nansen* in September 2008. This was the first multidisciplinary cruise covering the whole east Madagascar coast conducted by a vessel with up-to-date equipment for both physical and biological sampling.

The article is organized as follows: A description of the data and methods is given in Section 2. Observed current velocities, winds, horizontal distribution of surface properties, and vertical distribution of water masses are presented in Section 3. In Section 4, we discuss our findings in terms of the different dynamics of the northern and southern EMC branches, volume transports, and undercurrents. Finally, Section 5 presents a summary and conclusions.

2. Data, instruments, and methods

The cruise track and the CTD station numbers of the R/V *Dr. Fridtjof Nansen* survey presented in this study are shown in Figure 1(a). The sea surface temperature (SST) values based on in situ observations from the vessel (5 m depth) are also included, as well as the bathymetry. The cruise was conducted from south to north and lasted for about 3 weeks in September 2008; note the nonsynoptic nature of the observations (see Table 1). The observational program consisted of a detailed zigzag survey on the inner shelf interrupted by long transects across the shelf out to the deep ocean (>4,000 m). The track southeastward from station 966 (Fig. 1a) in the north and transect 4 in the south are included for completeness of the horizontal distribution maps, but in this article, we discuss mainly the cross-shelf transects along the east coast from the northern tip (transect 12) to the southeast

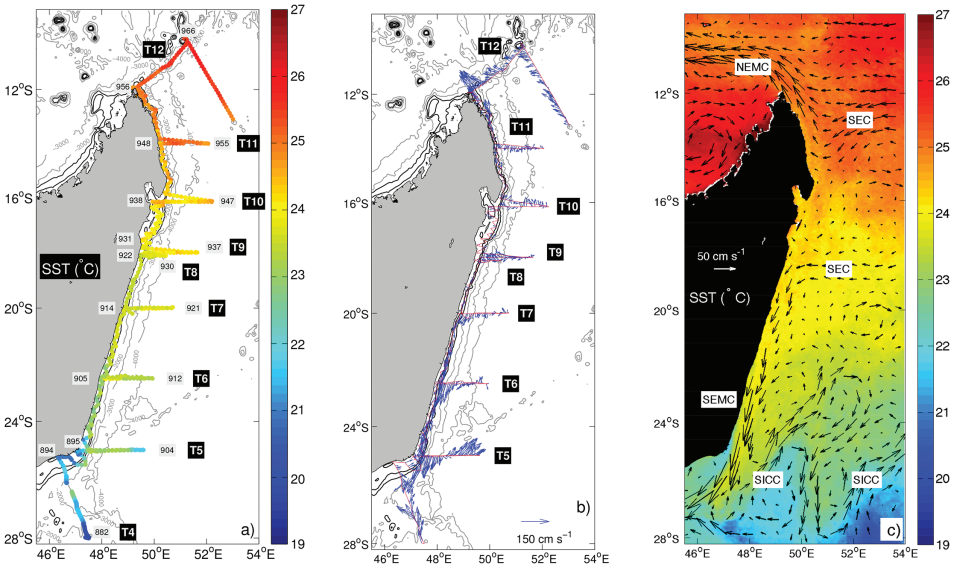

Figure 1. (a) Map of the study area and the cruise tracks with overlaid ship-based sea surface temperature (SST) observations. Labels indicate conductivity-temperature-depth stations and transects according to Table 1. Black contours highlight the isobaths of 200 and 1,000 m depth. (b) Current vectors from acoustic Doppler current profiler observations obtained at 44 m depth. The scale is indicated in the lower right-hand corner. (c) Altimeter-derived geostrophic circulation with overlaid SST from remotely sensed data averaged over September 2008. Labels indicate the South Equatorial Current (SEC), the North East Madagascar Current (NEMC), and the South East Madagascar Current (SEMC). Note that the pathway of the South Indian Ocean Countercurrent (SICC) is also suggested.

Table 1. List of the starting day (September 2008), time (GMT), and duration (hours) of transects 4–12 indicating the corresponding station number. See Figure 1 for positions of transects and station numbers.

Transect	Station	Day	Time	Duration
4	882	5	04	37
5	895	7	12	27
6	905	10	09	20
7	914	13	01	44
8	922	15	14	15
9	931	18	21	21
10	938	21	15	36
11	948	24	01	27
12	956	26	17	34

corner of Madagascar, where the coastline makes a sharp turn at Tôlanaro (25°02′S; transect 5).

a. Acoustic Doppler current profiler (ADCP)

A vessel mounted 150 kHz Ocean Surveyor ADCP from RD Instruments was running continuously during the cruise. The ADCP was set to ping synchronously with the echo sounder (Simrad ER60). In the postprocessing, the blanking distance was set to 14 m and the bin size was set to 12 m. The time averaging was set to 3 minutes.

All data reported from the firmware WinADCP with percent good (PG) less than 98 were eliminated. To avoid less reliable data, they were discarded when the ship was doing trawling or CTD work, the ship was steaming at less than 7 knots, the speed changed more than 2 knots, or the direction changed more than 10° during the 3-minute interval. An exception was made for the comparison with geostrophy, for which a PG threshold of 95 was applied and data from periods of low ship's speed were not excluded. The PG values dropped abruptly below 200 m so that we are using the data only from the upper range, although the nominal range was 350–400 m.

b. Thermosalinograph and fluorimeter

The thermosalinograph used during the survey was an SBE 21 SEACAT equipped with an in-line Turner Design SCUFA (self-contained underwater fluorescence apparatus) fluorometer measuring the sea surface fluorescence (SSF). The thermosalinograph was running continuously logging every 10 seconds using water from the cooling water intake located at 5 m depth. We will refer to the salinity measurements from the water intake as sea surface salinity (SSS). In the postprocessing, a running mean with filter length 1 hour was applied. All measurements when the ship was steaming at less than 7 knots were discarded. The salinity and fluorescence sensors were out of service for a few hours when the ship was at the northeast corner of Madagascar. Spikes were removed manually. Chlorophyll concentration was estimated from fluorescence using instrument calibration defaults. Because of the lack of in situ calibration, estimated chlorophyll values are considered only qualitatively.

c. SST

We complement the overview of SST provided with in situ measurements from the thermosalinograph with the monthly field of reprocessed satellite data for September 2008 from the MODIS Terra satellite on a 4 km grid scale (Feldman and McClain 2016).

d. CTD

The CTD profiler was a Seabird 911 plus system equipped with SBE 43 dissolved oxygen sensor and a Chelsea Mk III Aquatracka fluorimeter. The CTD was mounted on a SBE 32 carousel carrying Niskin bottles for water samples, which were used to calibrate

the conductivity and oxygen sensors. For further details, we refer to the cruise report (Krakstad et al. 2008).

e. Meteorological measurements

A shipborne PB100 (version WIMDA) meteorological station provided by AIRMAR was sampling during the whole cruise and logged the data every minute. The nominal height of the wind observations was 9 m. Note that for display of the data we use wind vectors instead of standard meteorological wind arrows.

f. Satellite altimeter data

The absolute dynamic topography (ADT) data used are the latest version of merged and gridded satellite altimeter observations produced by SSALTO/Data Unification and Altimeter Combination System (DUACS) and distributed by Archiving, Validation, and Interpretation of Satellite Oceanographic data (AVISO) with support from Centre national d'études spatiales (CNES) (DUACS 2014, v.15.0; SSALTO/DUACS 2015). The ADT is the result of adding sea level anomaly (SLA) to the new mean dynamic topography (MDT_CNES-CLS13) produced by the CLS Space Oceanography Division as an estimate of the ocean sea surface height above the geoid for the 1993–2012 period. We use the "all sat merged" series of ADT, which consists of a data set of daily maps on a 1/4° Cartesian grid where all missions available are considered and observations from up to four satellites at a given time are merged (Ducet, Le Traon, and Reverdin 2000).

Altimeter-derived velocities from maps of ADT were calculated assuming a geostrophic balance (i.e., a balance between Coriolis force and pressure gradient force):

$$u = -\frac{g}{f}\frac{\partial h}{\partial y}, \qquad v = \frac{g}{f}\frac{\partial h}{\partial x}, \tag{1}$$

where u is the zonal velocity (positive in the eastward direction), v is the meridional velocity (positive in the northward direction), h is the ADT, f is the Coriolis parameter for a given latitude, and g is the gravitational acceleration.

g. Models, tools, and calculations

The Modern Era Retrospective Analysis for Research and Applications (MERRA) (Rienecker et al. 2011) was used for reanalysis of wind data at 10 m height. The gridded spatial resolution was 50×50 km. The reanalysis contributes to a more synoptic picture of the wind fields during the cruise, and a monthly mean for September 2008 was used. Further details of the MERRA model are available at https://gmao.gsfc.nasa.gov/reanalysis/MERRA.

The tidal influence on the ADCP current meter observations were investigated using TPXO7.1: Global Inverse Tide Model (Egbert and Erofeeva 2002). The model tidal components were calculated for the time and position of the ADCP current measurements but were found to be small and were not removed from ADCP measurements.

Table 2. Volume transports perpendicular to transects 5 and 12 based on acoustic Doppler current profiler (ADCP) measurements and compared with geostrophic calculations with reference level at 176 m. In the "box method" the velocity is given a constant value between the vertical profiles, and for the "interpolation method" the values are linearly interpolated horizontally. CTD, conductivity-temperature-depth; NW, northwest; S, south.

	Transect 5 (134 km)	Transect 12 (156 km)
ADCP observations 14–182 m	9.9 Sv S	17.8 Sv NW
CTD "box method"	8.5 Sv S	16.6 Sv NW
CTD "interpolation method"	7.9 Sv S	17.3 Sv NW

Volume transports were computed from vertical geostrophic profiles, adjusted with ADCP current velocities, using two methods: in one (the "box method"), velocity is set to a constant value equal to the observed value in each depth bin between vertical profiles; in the other (the "interpolation method"), velocities are linearly interpolated in the horizontal. The difference between the results computed with the two methods (see Table 2) is the largest cause of uncertainty in the volume transport estimates. The contribution from error estimates of the ADCP measurements is small. Likewise, the difference between keeping the deepest measured velocity constant to the bottom (a calculation method we may refer to as full-slip) and letting velocities decrease to zero at the bottom (no-slip) makes only a small contribution toward the volume uncertainty. We will therefore use the difference between the results computed with the box and the interpolation methods to approximate the error of the volume transports.

The General Bathymetric Chart of the Ocean is applied. The oceanographic Matlab toolboxes Seawater, Ocean, and m_map by Rich Pawlowicz were used.

3. Results

a. Horizontal distribution of upper ocean properties, currents, and wind

Surface layer temperatures from in situ and remotely sensed data measured during the cruise show the expected meridional distribution with warmer water toward the equator (Fig. 1a and c). The corresponding horizontal distributions of upper layer (44 m depth) current velocities from the ADCP and altimeter-derived geostrophic velocities are presented in Figure 1(b) and (c), noting that remotely sensed data are averaged over the month of September 2008. On the whole, in situ and remotely sensed observations reveal the same current patterns, although, as expected, the ADCP snapshot observations are considerably stronger than the monthly averaged satellite currents.

In the main, the most dominant features not following the general pattern of temperature distribution were a warm tongue penetrating south-southwest in the southeast corner of Madagascar, flowing along the SEMC, and a relatively cooler tongue penetrating northward in the northeast corner of the island, flowing along the NEMC.

On the along-shore zigzag line (Fig. 1b), ADCP measurements show that currents were relatively weak between about 15° S and 20° S, and nearshore currents were in opposite directions north and south of about 19° S. This suggests that the bifurcation of the SEC, feeding downstream the SEMC and the NEMC, occurred roughly between transect 7 and transect 8 at the time of the cruise.

The SEMC warm tongue somewhat overshot the southeast corner of Madagascar, becoming separated from the coast at the point where the coastline makes a sharp turn. In this region, the colder inner shelf was dominated by surface countercurrents flowing northeastward (Fig. 1b and c). In transect 7 (20° S) and southward, the currents show a southbound jet, the SEMC, which was displaced some 20 km offshore from the coast, increasing to 50 km in transect 5.

The SEMC increased in strength and had its maximum velocity on transect 5 at 25° S, with core speeds above 150 cm s^{-1}. Outside of the SEMC, beyond 150 km offshore, currents turned toward the northeast. A trace of an equatorward return current was also observed in transects 6 and 7 but so much weaker that it is not clear whether it is a continuation of the feature in transect 5. Thus, the northeastward return current in transect 5 might be interpreted as part of the SICC (see Siedler, Rouault, and Lutjeharms 2006; Palastanga et al. 2007).

North of 19° S the current structure was different. A northbound current, the NEMC, was found near shore in all transects. It was typically about 20 cm s^{-1} in transects 9 and 10. In transect 11, the northward current was confined to the most nearshore part of the transect, whereas in transect 12, at the northern tip of Madagascar, the NEMC turned toward the northwest and formed an almost 100 km wide jet where the highest speed (160 cm s^{-1}) of the whole survey was observed.

In the SSS field (Fig. 2a), a tongue of less saline water can be seen following the warm water excursion in the southeast corner of Madagascar. In addition, there were patches of relatively fresh ($S \approx 34.8$) water south of transect 7 and more clearly around Nosy Mangabe (14°–18° S). These more brackish patches are probably influenced by river runoff. The Mangoro River, which is the largest river on the east coast of Madagascar (Knopp et al. 2011), has its mouth near 20.5° S and may be the source of the salinity minimum ($S \approx 34.2$) observed around transect 7. On the northeast coast (near transect 10), there are several rivers that contribute to freshening the surface layer. Low salinities were found from the mouth of the Bemarivo at about 14° S to the Maningory and Onibe Rivers just south of 17° S, and were most marked in a patch centered on the Antainambalana, which has its mouth within the Bay of Antongil at 15.75° S.

As mentioned in Section 2b, chlorophyll concentrations estimated from underway SSF data must be interpreted with caution in the absence of an in situ calibration of chlorophyll concentration. The horizontal SSF distribution (Fig. 2b) showed relatively low fluorescence over most of the sampled region, with the most notable exception being the nearshore band of significantly higher SSF values south of 22° S (maximum $\sim$1.3 μg L^{-1}), suggesting higher primary productivity in this region. The band of high SSF values was located inshore from

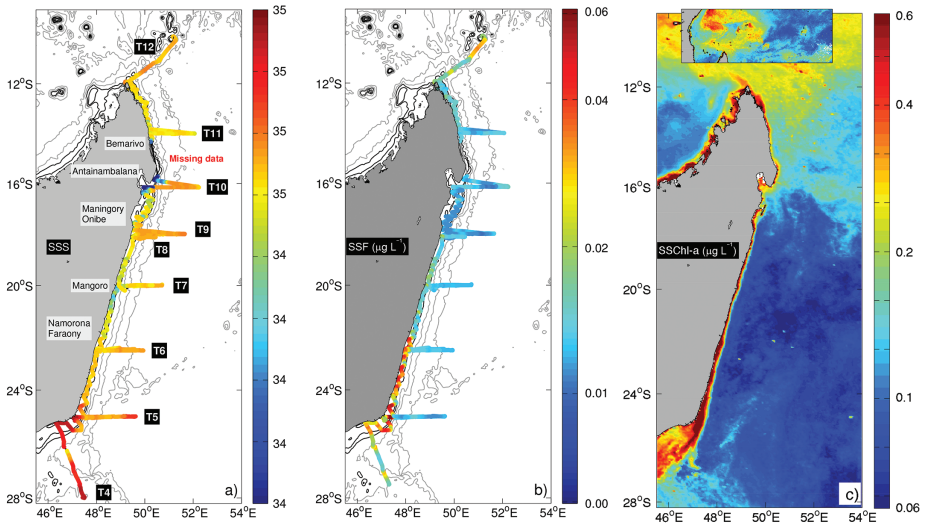

Figure 2. Horizontal maps of sea surface salinity (SSS) (a) and sea surface fluorescence (SSF; µg L^{-1}) (b) at 5 m depth from the thermosalinograph and fluorimeter. (c) Horizontal map of sea surface chl-*a* (SSChl-a; µg L^{-1}) from remote-sensed observations and time averaged for September 2008 (the inset map shows the chl-*a* bloom north of Madagascar and over the Seychelles Dome). Missing values between transect 10 and 11 in panels (a) and (b) are indicated.

the warm, low-salinity tongue following the path of the SEMC and leaving the coast at the southeast corner of Madagascar.

The wind observations obtained during the cruise are shown as blue vectors in Figure 3 together with the mean monthly wind fields for September 2008 obtained from the MERRA reanalysis. Because the MERRA winds represent monthly means, they appear weaker than the directly observed winds.

The bifurcation of the wind field at the east coast of Madagascar was displaced farther south for the observed winds (21° S) than the modeled wind (18.5° S). The MERRA wind field for August 2008 (not shown) representing the beginning of the cruise compares better with the observed wind observations in Figure 3, with the zonal wind hitting the coastline at 21° S. This suggests that the wind system might be migrating northward following the usual seasonal pattern of the SEC bifurcation latitude (see Chen et al. 2014).

South of the bifurcation point, the wind was southward along the southeast coast of Madagascar, therefore promoting upwelling, and increasing downstream toward the southeast corner of Madagascar. This is in agreement with the enhanced signal of SSF previously noted as inside of the warm, low-salinity tongue following the path of the SEMC (Fig. 2b). North of 21° S, the wind was northward parallel to the coast with the strongest winds in the northern part. This wind regime favors coastal downwelling due to Ekman transport toward the coast, a scenario that has been previously identified by Ponsoni, Aguiar-González,

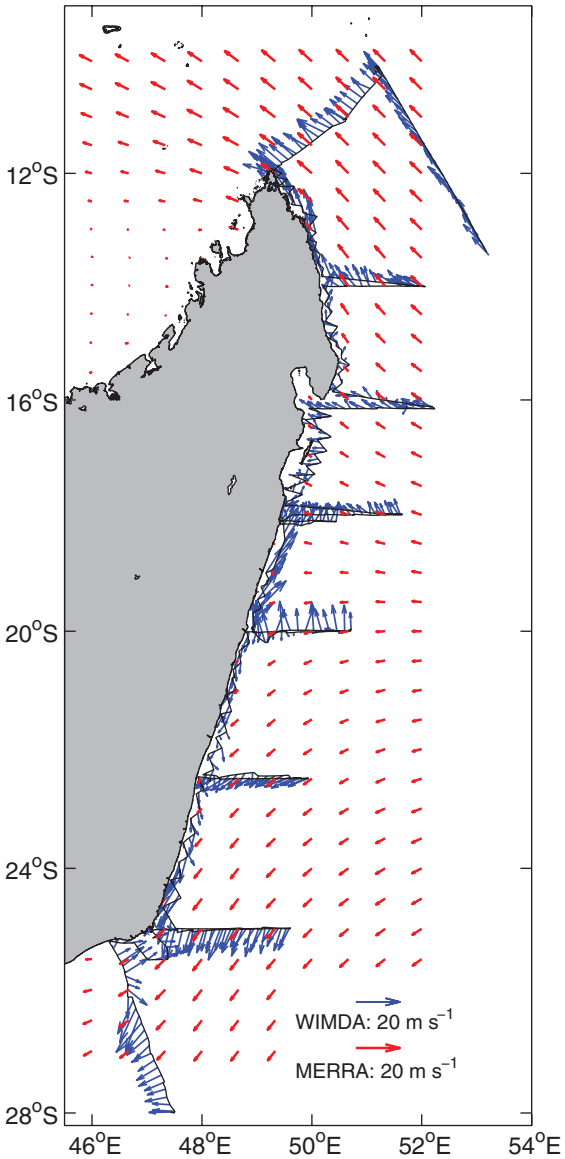

Figure 3. Wind observations (WIMDA) obtained onboard the vessel (blue arrows) and Modern Era Retrospective Analysis for Research and Applications (MERRA) monthly averaged wind field for September 2008. Velocity scales are shown in the lower right corner.

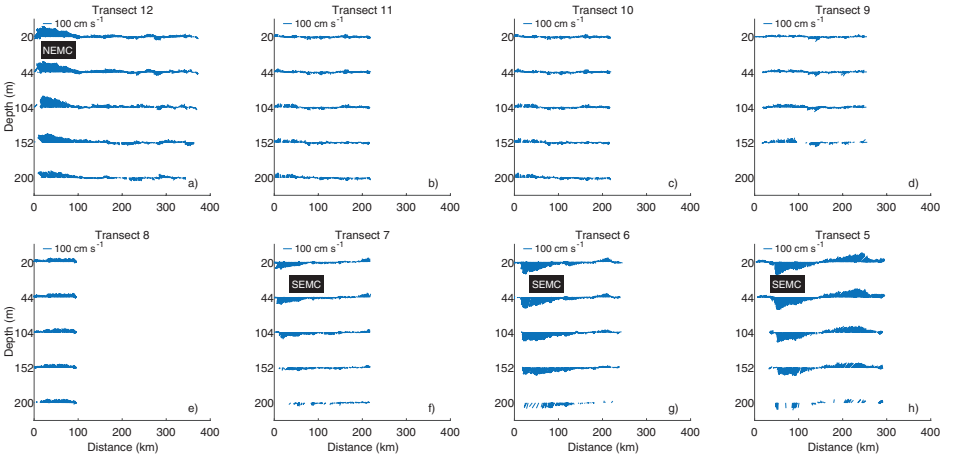

Figure 4. (a–h) Vertical velocity structure of the East Madagascar Current current system from ADCP measurements shown as velocity vectors from transect 12 to transect 5. Vectors refer here to north–south (up–down) and east–west (left–right) directions. Note that the distances along the y-axis are not to scale. Blank distances along the x-axis are missing values. For positions, see Figure 1. Labels indicate the North East Madagascar Current (NEMC) and the South East Madagascar Current (SEMC).

Nauw, et al. (2015) as an important contributor to the rise of strong baroclinic gradients and the likely development and persistence of the NMUC, flowing southeastward below and opposite to the surface NEMC.

The relatively higher values of SSF measured offshore at transect 12 agree well with remote-sensed patches of high sea surface chlorophyll north of Madagascar (Fig. 2b and c, see also the inset in panel c). At this time of the year, the Seychelles Dome, an open ocean upwelling site, is generally found at its southwesternmost location—namely, north of Madagascar (Xie et al. 2002; Aguiar-González et al. 2016). This phenomenon is most likely responsible for the horizontally spread region of enhanced remote-sensed chlorophyll reaching the northern coast of Madagascar during the sampling period.

b. Vertical current structure and volume transport

The current structure throughout the upper 200 m on all the transects is shown in Figure 4. The pattern of current velocities down to 200 m largely reflected those observed in the surface layer, although a downward weakening was noticeable where the surface currents were strong (see, e.g., Fig. 4a and f–h).

On the northernmost transect, 12 (Fig. 4a), a wide band of very strong current between about 10 km and 100 km offshore marked the presence of the NEMC. Although weaker than in the upper 50 m, current velocities at 152 m still exceeded 100 cm s^{-1} in the core of the NEMC. Farther offshore, currents on the northern transects were weaker and variable

throughout the upper 200 m. Along the northeast coast (transects 11, 10, 9, and 8), there was a band of consistent northward flow within the innermost 50–100 km that did not notably weaken with depth in the upper 200 m.

Between transects 8 and 7, there was a transition from northward to southward current in the 100 km nearest to shore. The southward current became stronger farther south, at transect 6, and was the strongest at transect 5. Offshore of the southward current branch (the SEMC), there was a band of northward current velocity—a thin band of relatively weak current centered at about 200 km offshore at transect 6 and a wider band of strong northeastward current at transect 5. One may associate the latter with the northeastward meandering current observed in Figure 1(c) from altimetry and here suggested to be part of the SICC at its generation area, where the regular presence of high mesoscale variability (Palastanga et al. 2007) may mask the mean flow. The strength of both the SEMC and the return current outside of ~140 km offshore decreased somewhat with depth. The downward weakening of the SEMC was noticeable during the cruise on all the southern transects (5, 6, and 7) and extended, at least, down to the deepest ADCP measurement (i.e., 200 m depth). In this regard, it is worth noting that Ponsoni, Aguiar-González, Nauw, et al. (2015) found the signal of the SEMC extends, on average, down to 1,000 m depth, while direct measurements from Ponsoni, Aguiar-González, Nauw, et al. (2015) found the vertical scale of the NEMC to be about 250 m over the shelf.

Hereafter we will focus mainly on the transects where the northern and southern branches of the EMC are the best developed, letting transect 12 represent the NEMC and transect 5 the SEMC.

The EMC system represents a major source of water for the Agulhas leakage to the Atlantic Ocean (Beal et al. 2011), and, therefore, an estimate of its volume transport contribution is of potential interest. In this work, we calculate direct estimates of the volume transports in the upper 200 m from the ADCP current measurements (see Table 2) and test the feasibility of calculating referenced geostrophic transports for deeper water layers for comparison with estimates from the literature (Table 3).

Figure 5 shows the comparisons between the measured and the referenced geostrophic currents for transects 5 and 12. The referenced geostrophic profiles have been adjusted to match the observed ADCP currents at 176 m depth. As a result, the vertical profiles, strength, direction, and positions of the different current properties compare well (Fig. 5). The fact that the horizontal structure of the near-surface ADCP currents (Fig. 1b) seems to match the structure revealed by the altimeter-derived geostrophic velocity fields (Fig. 1c) further supports the geostrophic approximation.

In Table 2, comparison of the ADCP-based and geostrophic transports for the upper 182 m on transects 5 and 12 shows that the calculations based on direct ADCP measurements are a little higher. However, this is expected as ADCPs measure total velocities, including the direct wind-driven currents, which, according to Figure 3, will contribute to increased transports; ADCPs include geostrophic and ageostrophic velocities, whereas the latter are absent in the geostrophic model. The good agreement has encouraged us to

Table 3. Comparison of volume transport estimates from literature and the present study, where the "interpolation method" is applied (see Table 2). Note also that estimates at 12° S and 25° S correspond, respectively, to transect 12 and transect 5 for the present study. Full-slip is applied near the bottom (i.e., the deepest velocity value is kept constant to the bottom). ADCP, acoustic Doppler current profiler; LADCP, lowered acoustic Doppler current profiler; RCM, Recording Current Meter.

	Swallow, Fieux, and Schott (1988)	Schott et al. (1988)	Nauw et al. (2008)	Ponsoni, Aguiar-González, Nauw, et al. (2015); Ponsoni et al. (2016)	This study
Methodology	Ref. level no motion	RCM	LADCP	LADCP ‖ RCM, ADCP	Ref. to ADCP
Position (°S)	12 ‖ 23	12 ‖ 23	– ‖ 25	12 ‖ 23	12 ‖ 25
Reference depth (m)	1,100 ‖ 1,170	– ‖ –	– ‖ –	– ‖ –	176 ‖ 176
Transect length (km)	115 ‖ 110	115 ‖ 110	– ‖ 160	90 ‖ 115	142 ‖ 105
Depth of integration (m)	1,100 ‖ 1,170	1,100 ‖ 1,170	– ‖ 1,100	2,500 ‖ 3,950	1,100 ‖ 1,100
Volume transport (Sv)	30 ‖ −21	27 ‖ −20	– ‖ −30	34 ‖ −18	48 ‖ −22

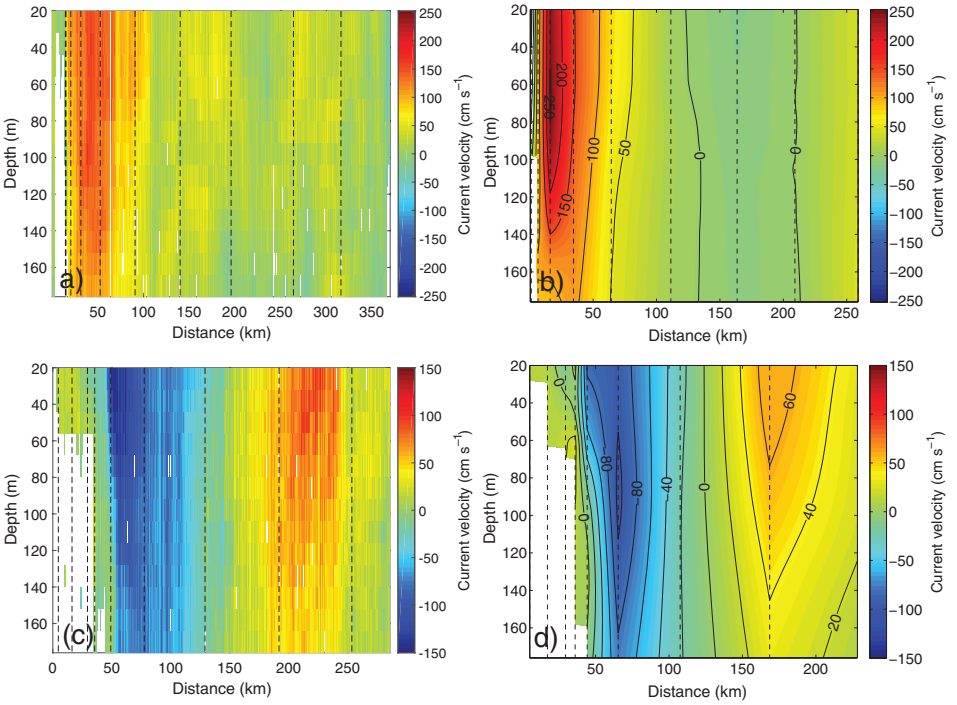

Figure 5. Observed currents (a, c) and referenced geostrophic current fields (b, d) for transect 12 (upper panels) and transect 5 (lower panels). The geostrophic currents are adjusted to match the acoustic Doppler current profiler observations at 176 m depth. Positive currents are toward the northwest in transect 12 and the north in transect 5.

use the geostrophic approximation to estimate the transport for deeper layers as well. The geostrophic transects for the inner parts of transect 12 defining the NEMC and transect 5 defining the SEMC, as well as the geostrophic profiles for the whole sections, are shown in Figure 6. The corresponding transport estimates are compared with the literature in Table 3.

Through transect 12 (12° S) our estimate of the NEMC volume transport is higher (48 ± 4 Sv) than earlier values reported in the literature (Table 3). This may be because of the strong influx of a northern branch of the SEC acting during the period of sampling (see Fig. 1c).

Through transect 5, we obtained a volume transport of 22 ± 3 Sv, which agrees better with earlier estimates (Table 3) and confirms southward transport of about 20–30 Sv. If we calculate the transport here using 3,000 m as the integration depth to compare with the results of Ponsoni et al. (2016), we get 19 ± 7 Sv, close to their estimate of 18 Sv.

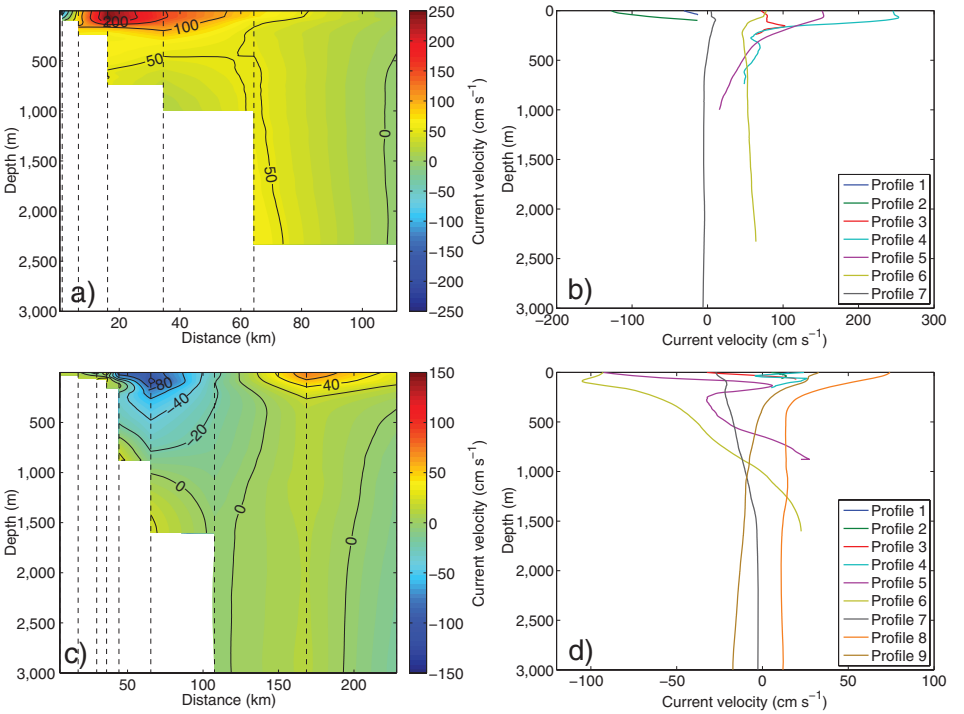

Figure 6. Geostrophic velocity distributions of inner parts (a, c) and geostrophic velocity profiles (b, d) for transect 12 (upper panels) and transect 5 (lower panels). Positive currents are toward the northwest in transect 12 and the north in transect 5. The geostrophic currents are adjusted to match the acoustic Doppler current profiler observations at 176 m depth. Profile 1 is close to the shore.

c. Water mass properties

Figures 7 and 8 show the vertical distributions of potential temperature, salinity, and oxygen for all transects, which in combination with the θ/S and θ/O_2 diagrams in Figure 9 present the water mass distribution of the EMC system according to water mass definitions in Emery and Meincke (1986) and Emery (2001). To ease discussion, a legend with water mass properties of each transect has been added in Figure 9(a) and (c), and depths are indicated in panel (b).

Below the high-salinity and low-oxygen Subtropical Surface Water at about 250 m depth, oxygen-rich South Indian Central Water (SICW) was found between 300 and 800 m in the southernmost transects. Farther north, the layer of SICW was thinner, diluted, and lifted up (Figs. 7–9). Below the SICW, centered at about 1,000 m, there was a minimum salinity layer, more clearly defined in the south than in the north. In the same depth range as the salinity minimum, there was an oxygen minimum layer, which was more dominant in the north than in the south (Figs. 7 and 8). The water in this intermediate layer marked by

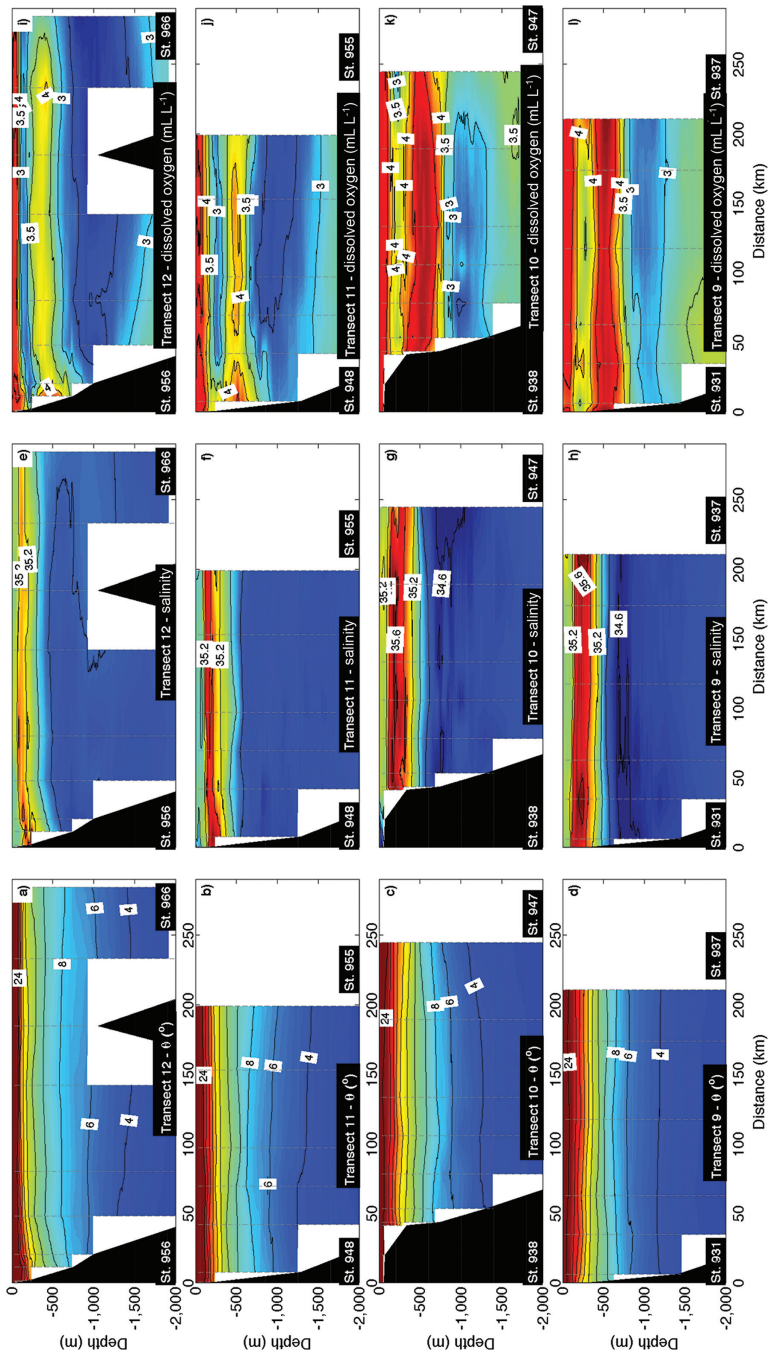

Figure 7. Vertical sections of potential temperature (first column, °C), salinity (second column), and dissolved oxygen (third column, mL L^{-1}). Transects are presented from north to south (i.e., from transect 12 [upper panels] toward transect 9 [lower panels]). In each panel, start and end numbers of conductivity-temperature-depth stations are also indicated.

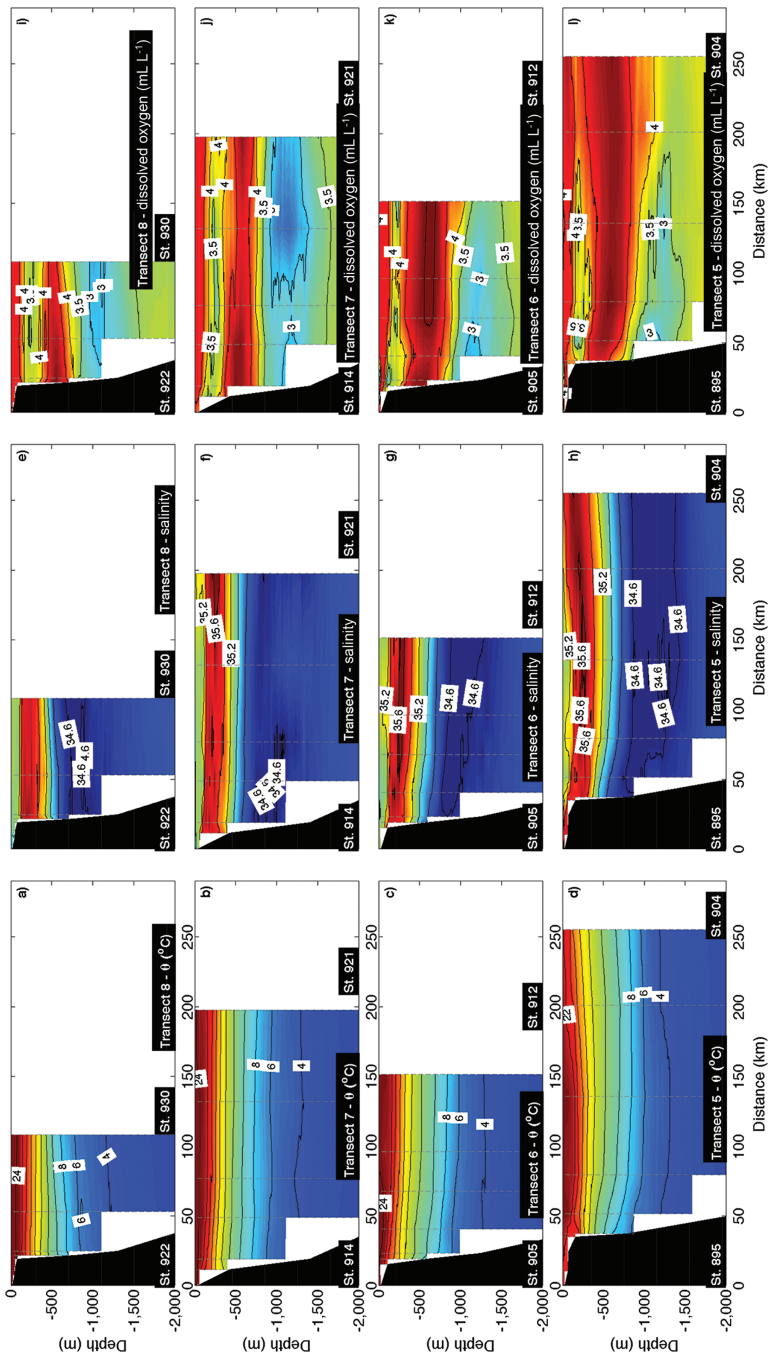

Figure 8. Same as Figure 7 but for transect 8 toward transect 5 (i.e., from north to south).

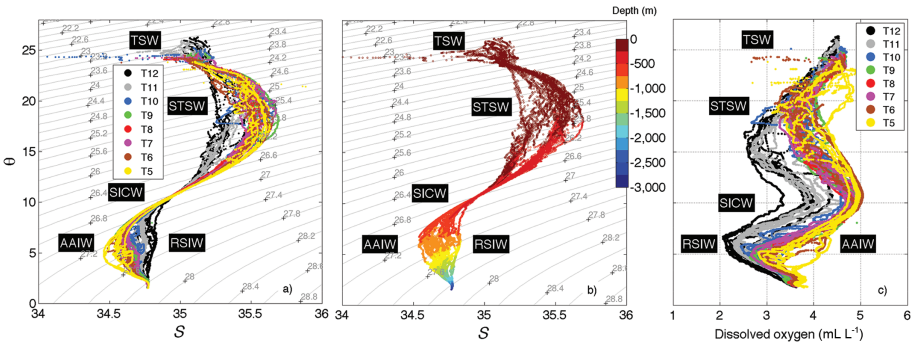

Figure 9. The θ/S (a, b) and θ/O_2 (c) diagrams. In panels (a) and (c), colors represent the different transects (see the legend), and in panel (b), the color bar represents depth. Labels indicate acronyms for water masses AAIW, Antarctic Intermediate Water; RSIW, Red Sea Intermediate Water; SICW, South Indian Central Water; STSW, Subtropical Surface Water; TSW, Tropical Surface Water.

salinity and oxygen minima is identified as a mixture of the fresh and relatively oxygen-rich Antarctic Intermediate Water (AAIW), and the saline and oxygen-depleted Red Sea Intermediate Water (RSIW). The gradual transition from the dominance of RSIW on the northern transects to that of AAIW in the south can be seen in the θ/S and θ/O_2 diagrams (Figs. 9a and c). The θ/S diagram also shows sharp gradients and reversals indicative of interleaving, characteristic for regions where water masses with strongly differing salinities within the same density range come together.

Ponsoni, Aguiar-González, Maas, et al. (2015), who used data from a large number of Argo floats, also observed an increased influence of RSIW near the northeast coast of Madagascar, which is closer to the Red Sea outflow. In transect 5, near the southeast coast of Madagascar, the signs of RSIW were found closest to the continental slope, whereas the higher-oxygen and lower-salinity AAIW was observed in the outer part of the transect. Farther north, in transects 6 and 7, a similar oxygen minimum was found seemingly leaning on the slope, bounded by somewhat higher oxygen concentrations offshore. The nearshore RSIW observed on the southernmost transects might have come from the Mozambique Channel and been transported northward by the northbound EMUC, which is also located at ~1,000 m depth in this region (Nauw et al. 2008; Ponsoni, Aguiar-González, Maas, et al. 2015). On transect 7, however, a stronger and thicker oxygen minimum layer is found even farther offshore, and on most transects north of this, the RSIW is present as a more or less continuous layer dominating the water column below and offshore of the core of SICW.

For a closer look at the upper 500 m of the water column, the reader is referred to Figures S1 and S2 in the supplementary material, where the vertical distributions of potential density, salinity, and chlorophyll are shown. In those, the highest concentrations of chlorophyll were also found off the southeastern coast, where a maximum hugging the slope was located in all transects inshore from the isopycnals supporting the SEMC (Fig. S2, see

first and third columns). This location of the chlorophyll maxima agrees well with surface remotely sensed data in Figs. 2(b) and (c). Along the northeastern coast, the highest values of chlorophyll were found northward and offshore, where closeness to the Seychelles Dome upwelling site seems to be the most likely cause.

4. Discussion

a. The different dynamics of the SEMC and the NEMC

The dominating wind direction in the area east of Madagascar is zonal, and the corresponding wind stress vorticity ζ (the zonal component of the wind stress curl) may be computed as $\zeta = \frac{\partial \tau_X}{\partial y}$ where τ_x is the zonal wind stress. During the time of the cruise, in situ observations of the near-surface wind field suggest that ζ drops to zero at $\sim$21° S (Fig. 3, blue arrows), the latitude at which, according to Sverdrup theory, the meridional water transport vanishes and a maximum westward transport is expected with a corresponding bifurcation of the ocean currents. Our ADCP measurements (Fig. 1b) and the satellite-derived surface geostrophic fields (Fig. 1c) show, however, that the ocean current bifurcated farther north at 19° S. These observations thus contrast with the finding of Chen et al. (2014) that the ocean current bifurcation occurs 0.8° poleward of the zero wind stress curl line because of Godfrey's island rule. The discrepancy may be because of the different timescales involved, in our case the week-to-week changes, whereas Chen et al. (2014) studied seasonal and interannual variability. The monthly averaged MERRA wind field (Fig. 3, red arrows) suggests a more northerly location of the zero ζ line at $\sim$18.5° S, in closer agreement with the observed bifurcation latitude of the SEC.

The strong horizontal velocity gradient of the SEMC shown in Figures 1(b) and 4 with a maximum at about 50 km offshore and weaker currents toward the coast is characteristic for western boundary currents, in which horizontal and vertical shears are typically strongest on the inshore side (Imawaki et al. 2013).

The NEMC presented the structure of a narrow nearshore jet out to about 100 km offshore, outside of which currents were weak. The vertical profiles of velocity (Fig. 4) show a unidirectional flow with a strong vertical shear in the upper 200 m aligned with the topography. This is an example showing that topographic steering because of conservation of potential vorticity holds even in stratified water (Svendsen, Sætre, and Mork 1991; Marshall 1995). The intensification of the NEMC at the northern tip of Madagascar appears in this study to be promoted by a strong influx of a northern branch of the SEC (see Fig. 1c), a recurrent contributor of the NEMC as captured in altimeter-based seasonal climatologies of the southern Indian Ocean (Aguiar-González et al. 2016).

On the southernmost transect, transect 5, isopycnals in the upper 200 m deepened toward about 120 km from the coast (Fig. S2d). The upward slope on the offshore side of the bowl-shaped isopycnals is roughly colocated with the zero velocity line (at about 150–160 km offshore) between the southward SEMC on the inner part of the transect and the meandering northeastward flow, which reaches a maximum at about 220 km offshore (Fig. 4h).

The SICC appears in geostrophic surface current fields as a zonal band of high mesoscale variability, centered on 25° S, where a mean zonal countercurrent emerges in multiyear averages and is continuous at least out to 80° E (Siedler, Rouault, and Lutjeharms 2006; Palastanga et al. 2007). The shallow eastward jet of the SICC is associated with the front between Tropical and Subtropical Surface Water (Nauw et al. 2008), and as it flows above the SEC, it fulfills conditions for baroclinic instability, which explains the high eddy variability (Palastanga et al. 2007). Thus, the northeastward current in the outer part of transect 5 (Figs. 1b and c, and 4h) may be interpreted as the SICC or as a local eddy. If the latter, it forms part of the eddy flow pattern along ∼25° S and can still be considered as an element of the SICC, as previously suggested in Sections 3a and 3b.

On the northernmost transect, transect 12, the density structure (isopycnals following the isotherms) showed strong baroclinicity close to the coast (Fig. S1a). As advanced in Section 3a, this was also observed by Ponsoni, Aguiar-González, Nauw, et al. (2015), who explained it by a wind-driven onshore Ekman transport causing the down-dipping of the isotherms close to the shore. This explains the baroclinic structure of the nearshore ADCP current fields, which shows a velocity difference of about 50 cm s^{-1} in the upper 200 m (Fig. 4a). The fluorescence values in transect 12 were low (Fig. 2b), suggesting low biological production.

b. Undercurrents

The vertical geostrophic profiles obtained at transect 5 (25° S) show an equatorward current below 900 m depth close to the slope (Fig. 6d); these velocity profiles (profiles 5 and 6) present velocities toward north above 20 cm s^{-1}. This compares well with observations by Nauw et al. (2008) and Ponsoni, Aguiar-González, Maas, et al. (2015), confirming the existence of the EMUC. These authors found that 20 cm s^{-1} was close to the maximum speed obtained during the observation period for the EMUC. They argued that the maxima of the EMUC were related to a barotropic contribution originated from the interaction with westward-propagating cyclonic eddies arriving to the southeastern coast of Madagascar. Ponsoni, Aguiar-González, Maas, et al. (2015) calculated the average transport of the EMUC to be 1.3 Sv with maximum near 6 Sv, which roughly agrees with the 3.1 ± 1 Sv obtained in this study.

A southeastward undercurrent at the northern tip of Madagascar (NMUC) was recently discovered by Ponsoni, Aguiar-González, Nauw, et al. (2015) centered at about 450 m depth and hugging the slope at about 10 km from the shore. The adjusted geostrophic profiles presented here (Fig. 6a and b) do not show an undercurrent. Nevertheless, we note that below the northwestward-flowing core of the NEMC at the surface, geostrophic velocity profiles 3–5 exhibit a clear downward decrease toward a minimum at depth, although the minimum currents are still here above 50 cm s^{-1}. In this latter context, it is worth noting that Ponsoni, Aguiar-González, Nauw, et al. (2015) observed a speed difference of 120 cm s^{-1} between the core of the NMUC at 450 m and the surface current, which is

comparable to the shear observed here (see Fig. 6b). In line with this, one may reasonably argue that the NMUC might be masked during the cruise time because of the strong contribution of barotropic northwestward flows coming from the SEC, as suggested from the altimeter-derived circulation (Fig. 1c). This scenario agrees with the relatively strong NEMC transport obtained in this work when compared with volume transport estimates reported in the literature (see Table 3), although it might also be that the NMUC is an intermittent feature.

Interestingly, Ponsoni, Aguiar-González, Nauw, et al. (2015) found that the NMUC is carrying warm and saline water as the downwelling was tilting the isotherms and isohalines downward toward the slope. This was also the case during the cruise presented here (Fig. S1a and e).

5. Summary and conclusions

When the SEC hits the Madagascar coast, the water level near the coast will tend to rise, thus causing pressure forces poleward south of, and equatorward north of, the bifurcation point. In addition, the southward winds south of this point will cause the sea surface to slope down toward the coast, leading to southward geostrophic flows (Fig. 1b and c, and 3). Conversely, north of the bifurcation point, northward winds cause upsloping sea surface near the coast and northward geostrophic flows (Fig. 1b and c, and 3).

The alongshore winds south of the SEC bifurcation latitude tend to stimulate upwelling and down-dipping of the sea surface close to the shore, setting up a pressure gradient that causes a polar-bound geostrophic component of the current near the southeast coast where frictional forces may also be important. At the northeast coast, a corresponding coastal uptilting was forcing an equatorward current. However, in spite of the similar and symmetric coastal wind forcing, the current patterns of the NEMC and SEMC differ significantly. A coastal upwelling regime prevails along the SEMC, whereas the nature of the NEMC is downwelling.

According to the previous discussion, we may expect higher biological production at the southeast coast than in the north, and this was indeed confirmed by the SSF distribution (Fig. 2b). In addition, previous studies have suggested that deepening of the mixed layer because of westward-propagating eddies and/or Rossby waves (Longhurst 2001) and eddies shed from the SEMC off southern Madagascar (Srokosz et al. 2015) might also play an important role in enhancing biological production in this region by increasing the supply of nutrients to the photic zone.

Along the northeast coast, the biological production seemed to be stimulated by high-nutrient river runoff (Fig. 2a) and the closeness to the Seychelles Dome (Fig. 2b and c), an open ocean upwelling site that migrates near the northern coast of Madagascar during austral winter (Xie et al. 2002; Aguiar-González et al. 2016).

The volume transport carried by the SEMC was estimated to be 22 Sv toward the south through transect 5 (Table 3). Below the SEMC, we observed the EMUC centered at about

1,100 m depth and flowing above the 1,500 m isobath with a maximum velocity component toward the north of about 20 cm s^{-1} (Fig. 6). According to our calculations, the transport in the EMUC was 3.1 ± 1 Sv, which is a little higher than the mean value (1.3 Sv) observed by Ponsoni, Aguiar-González, Maas, et al. (2015), but still within the range of their estimates. Farther east, about 150 km from the shore, a northeastward current was observed at transect 5 (see Figs. 1b, and c, and 4h), which we identify as the SICC (Nauw et al. 2008).

For the NEMC passing the tip of Madagascar, we obtained a very high transport (48 ± 4 Sv) compared with earlier estimates (see Table 3). This was probably because of a strong inflow of the SEC hitting the Madagascar coast at about 13° S (see Fig. 1c). Ponsoni, Aguiar-González, Nauw, et al. (2015) recently discovered an undercurrent below the NEMC, which they named the NMUC, located at about 10 km from the coast and centered at about 500 m depth. We did not observe such a return current, but a minimum velocity and a similar vertical velocity shear between surface and subsurface flows for the depths in question. These might be a footprint of the NMUC.

Downstream, the NEMC is believed to feed the anticyclonic eddies dominating the volume transport in the Mozambique Channel, which carries a net poleward flow of 17 Sv (Backeberg and Reason 2010; Ridderinkhof et al. 2010). On the other hand, the SEMC (18 Sv) feeds the Agulhas Current system through a southwestward-directed mean flow and anticylones and cyclones shedding off southern Madagascar (Chapman et al. 2003; de Ruijter et al. 2004; Ridderinkhof et al. 2013; Ponsoni et al. 2016). In the greater picture, the EMC system is a significant water source of the Agulhas Current system, which eventually leaks warm and saline water into the Atlantic Ocean via the shedding of Agulhas rings. The Agulhas Current itself carries about 70 Sv (Bryden and Beal 2001), and its warm, saline outflux has been suggested to modulate the Atlantic meridional ocean circulation (Beal et al. 2011; Simon et al. 2015). We think that future observational research on the EMC should be encouraged as it will benefit our basic understanding of the world ocean circulation and climate.

Acknowledgments. Data presented were collected by the EAF-Nansen project, http://www.fao.org/in-action/eaf-nansen/en, a partnership between the Food and Agriculture Organization of the United Nations, the Norwegian Agency for Development Cooperation, and the Institute of Marine Research. The survey was conducted in collaboration with the South West Indian Ocean Fisheries Project and the Agulhas and Somali Current Large Marine Ecosystems project. Satellite altimeter data used in this work were produced by SSALTO/DUACS and distributed by AVISO with support from CNES (http://www.aviso.oceanobs.com/duacs/). MERRA was developed by the Global Modeling and Assimilation Office and supported by the NASA Modeling, Analysis, and Prediction Program. Source data files can be acquired from the Goddard Earth Science Data Information Services Center. We also acknowledge the Ocean Biology Processing Group for SST data access (https://oceancolor.gsfc.nasa.gov/). The authors would like to thank Piers Chapman and two anonymous reviewers for their comments that helped significantly improve the manuscript. The second author also wishes to acknowledge the financial support from the Netherlands Organization for Scientific Research, section Earth and Life Sciences, through the ZKO Grant No. 839.08.431 awarded to the INATEX ("Indian-Atlantic exchange in present and past climate") program.

REFERENCES

Aguiar-González, B., L. Ponsoni, H. Ridderinkhof, H. M. van Aken, W. P. M. de Ruijter, and L. R. M. Maas. 2016. Seasonal variation of the South Indian tropical gyre. Deep Sea Res., Part I, *110*, 123–140. doi: 10.1016/j.dsr.2016.02.004

Backeberg, B. C., and C. J. C. Reason. 2010. A connection between the South Equatorial Current north of Madagascar and Mozambique Channel eddies. Geophys. Res. Lett., *37*, L04604. doi: 10.1029/2009GL041950

Beal, L. M., W. P. M. De Ruijter, A. Biastoch, R. Zahn, and SCOR/WCRP/IAPSO Working Group. 136. 2011. On the role of the Agulhas system in ocean circulation and climate. Nature, *472*(7344), 429–436. 10.1038/nature09983

Biastoch, A., C. W. Böning, F. U. Schwarzkopf, and J. R. E. Lutjeharms. 2009. Increase in Agulhas leakage due to poleward shift of Southern Hemisphere westerlies. Nature, *462*(7272), 495–498. doi: 10.1038/nature08519

Boyer, T. P., J. I. Antonov, O. K. Baranova, H. E. Garcia, D. R. Johnson, R. A. Locarnini, A. V. Mishonov, et al. 2009. World Ocean Database 2009: NOAA Atlas NESDIS 66, S. Levitus, ed. Washington, DC: U.S. Government Printing Office. http://www.vliz.be/imisdocs/publications/252058.pdf

Bryden, H. L., and L. M. Beal. 2001. Role of the Agulhas Current in Indian Ocean circulation and associated heat and freshwater fluxes. Deep Sea Res., Part I, *48*(8), 1821–1845. doi: 10.1016/S0967-0637(00)00111-4

Chapman, P., S. F. Di Marco, R. E. Davis, and A. C. Coward. 2003. Flow at intermediate depths around Madagascar based on ALACE float trajectories. Deep Sea Res., Part II, *50*(12–13), 1957–1986. doi: 10.1016/S0967-0645(03)00040-7

Chen, Z., L. Wu, B. Qiu, S. Sun, and F. Jia. 2014. Seasonal variation of the South Equatorial Current bifurcation off Madagascar. J. Phys. Oceanogr., *44*(2), 618–631. doi: 10.1175/JPO-D-13-0147.1

de Ruijter, W. P. M., H. M. van Aken, E. J. Beier, J. R. E. Lutjeharms, R. P. Matano, and M. W. Schouten. 2004. Eddies and dipoles around South Madagascar: Formation, pathways and large-scale impact. Deep Sea Res., Part I, *51*(3), 383–400. doi: 10.1016/j.dsr.2003.10.011

Ducet, N., P. Y. Le Traon, and G. Reverdin. 2000. Global high-resolution mapping of ocean circulation from TOPEX/Poseidon and ERS-1 and-2. J. Geophys. Res.: Oceans, *105*(C8), 19477–19498. doi: 10.1029/2000JC900063

Egbert, G. D., and S. Y. Erofeeva. 2002. Efficient inverse modeling of barotropic ocean tides. J. Atmos. Oceanic Technol., *19*(2), 183–204. doi: 10.1175/1520-0426(2002)019<0183:EIMOBO>2.0.CO;2

Emery, W. J. 2001. Water types and water masses, *in* Encyclopedia of Ocean Sciences, Vol. 6, J. H. Steele, K. K. Turekian, and S. A. Thorpe, eds. San Diego, CA: Academic Press, 3179–3187.

Emery, W. J., and J. Meincke. 1986. Global water masses: Summary and review. Oceanol. Acta, *9*(4), 383–391.

Feldman, G. C., and C. R. McClain. 2016. OceanColor Web, Terra MODIS Reprocessing Level 3, N. Kuring and S. W. Bailey, eds. Greenbelt, MD: NASA Goddard Space Flight Center. https://oceancolor.gsfc.nasa.gov/

Halo, I., B. Backeberg, P. Penven, I. Ansorge, C. Reason, and J. E. Ullgren. 2014. Eddy properties in the Mozambique Channel: A comparison between observations and two numerical ocean circulation models. Deep Sea Res., Part II, *100*, 38–53. doi: 10.1016/j.dsr2.2013.10.015

Harlander, U., H. Ridderinkhof, M. W. Schouten, and W. P. M. de Ruijter. 2009. Long-term observations of transport, eddies, and Rossby waves in the Mozambique Channel. J. Geophys. Res.: Oceans, *114*, C02003. doi: 10.1029/2008JC004846

Imawaki, S., A. S. Bower, L. Beal, and B. Qiu. 2013. Western boundary currents, *in* Ocean Circulation and Climate: A 21st Century Perspective, Vol. 103, G. Siedler, S. M. Griffies, J. Gould, and J. A. Church, eds. Amsterdam: Elsevier, 305–338.

Knopp, T., P. Rahagalala, M. Miinala, and I. Hanski. 2011. Current geographical ranges of Malagasy dung beetles are not delimited by large rivers. J. Biogeogr., *38*(6), 1098–1108. doi: 10.1111/j.1365-2699.2010.02463.x

Krakstad, J.-O., S. Mehl, R. Roman, J. Escobar-Porras, J. Stapley, B. Flynn, M. Olsen, and I. M. Beck. 2008. East Madagascar Current Ecosystem Survey: 23 August-01 October 2008. Bergen, Norway: Institute of Marine Research. http://www.nb.no/idtjeneste/URN:NBN:no-bibsys_brage_49233

Lambert, E., D. Le Bars, and W. P. M. de Ruijter. 2016. The connection of the Indonesian Throughflow, South Indian Ocean Countercurrent and the Leeuwin Current. Ocean Sci., *12*(3), 771–780. doi: 10.5194/os-12-771-2016

Longhurst, A. 2001. A major seasonal phytoplankton bloom in the Madagascar Basin. Deep Sea Res., Part I, *48*(11), 2413–2422. doi: 10.1016/S0967-0637(01)00024-3

Lutjeharms, J. R. E. 2006. The coastal oceans of south-eastern Africa (15,W), *in* The Sea, Vol. 14, Interdisciplinary Regional Studies and Syntheses, A. R. Robinson and K. H. Brink, eds. Cambridge, MA: Harvard University Press, 783–834.

Lutjeharms, J. R. E., A. Biastoch, P. M. van der Werf, H. Ridderinkhof, and W. P. M. de Ruijter. 2012. On the discontinuous nature of the Mozambique Current. S. Afr. J. Sci., *108*(1–2), 1–5. http://hdl.handle.net/10520/EJC97195

Lutjeharms, J. R. E., W. P. M. de Ruijter, H. Ridderinkhof, H. van Aken, C. Veth, P. J. van Leeuwen, S. S. Drijfhout, J. H. F. Jansen, and G.-J. A. Brummer. 2000. MARE and ACSEX: New research programmes on the Agulhas Current system. S. Afr. J. Sci., *96*(3), 105–110.

Marshall, D. 1995. Influence of topography on the large-scale ocean circulation. J. Phys. Oceanogr., *25*, 1622–1635. doi: 10.1175/1520-0485(1995)025%3C1622:IOTOTL%3E2.0.CO;2

Menezes, V. V., H. E. Phillips, A. Schiller, N. L. Bindoff, C. M. Domingues, and M. L. Vianna. 2014. South Indian Countercurrent and associated fronts. J. Geophys. Res.: Oceans, *119*(10), 6763–6791. doi: 10.1002/2014JC010076

Menezes, V. V., H. E. Phillips, M. L. Vianna, and N. L. Bindoff. 2016. Interannual variability of the South Indian Countercurrent. J. Geophys. Res.: Oceans, *121*(5), 3465–3487. doi: 10.1002/2015JC011417

Nauw, J. J., H. M. van Aken, J. R. E. Lutjeharms, and W. P. M. de Ruijter. 2006. Intrathermocline eddies in the Southern Indian Ocean. J. Geophys. Res.: Oceans, *111*, C03006. doi: 10.1029/2005JC002917

Nauw, J. J., H. M. van Aken, A. Webb, J. R. E. Lutjeharms, and W. P. M. de Ruijter. 2008. Observations of the southern East Madagascar Current and undercurrent and countercurrent system. J. Geophys. Res.: Oceans, *113*, C08006. doi: 10.1029/2007JC004639

Palastanga, V., P. J. Van Leeuwen, M. W. Schouten, and W. P. M. De Ruijter. 2007. Flow structure and variability in the subtropical Indian Ocean: Instability of the South Indian Ocean Countercurrent. J. Geophys. Res.: Oceans, *112*, C01001. doi: 10.1029/2005JC003395

Ponsoni, L., B. Aguiar-González, L. R. M. Maas, H. M. van Aken, and H. Ridderinkhof. 2015. Long-term observations of the East Madagascar Undercurrent. Deep-Sea Res., Part I, *100*, 64–78. doi: 10.1016/j.dsr.2015.02.004

Ponsoni, L., B. Aguiar-González, J. J. Nauw, H. Ridderinkhof, and L. R. M. Maas. 2015. First observational evidence of a North Madagascar Undercurrent. Dyn. Atmos. Oceans, *72*, 12–20. doi: 10.1016/j.dynatmoce.2015.08.002

Ponsoni, L., B. Aguiar-González, H. Ridderinkhof, and L. R. M. Maas. 2016. The East Madagascar Current: Volume transport and variability based on long-term observations. J. Phys. Oceanogr., *46*(4), 1045–1065. doi: 10.1175/JPO-D-15-0154.1

Ridderinkhof, H., and W. P. M. de Ruijter. 2003. Moored current observations in the Mozambique Channel. Deep Sea Res., Part II, *50*(12), 1933–1955. doi: 10.1016/S0967-0645(03)00041-9

Ridderinkhof, H., P. M. van der Werf, J. E. Ullgren, H. M. van Aken, P. J. van Leeuwen, and W. P. M. de Ruijter. 2010. Seasonal and interannual variability in the Mozambique Channel from moored current observations. J. Geophys. Res.: Oceans, *115*, C06010. doi: 10.1029/2009JC005619

Ridderinkhof, W., D. Le Bars, A. S. von der Heydt, and W. P. M. de Ruijter. 2013. Dipoles of the South East Madagascar Current. Geophys. Res. Lett., *40*(3), 558–562. doi: 10.1002/grl.50157

Rienecker, M. M., M. J. Suarez, R. Gelaro, R. Todling, J. Bacmeister, E. Liu, M. G. Bosilovich, et al. 2011. MERRA: NASA's modern-era retrospective analysis for research and applications. J. Clim., *24*(14), 3624–3648. doi: 10.1175/JCLI-D-11-00015.1

Sætre, R., and A. J. Da Silva. 1984. The circulation of the Mozambique Channel. Deep-Sea Res., Part A, *31*(5), 485–508. doi: 10.1016/0198-0149(84)90098-0

Schott, F., M. Fieux, J. Kindle, J. Swallow, and R. Zantopp. 1988. The boundary currents east and north of Madagascar: 2. Direct measurements and model comparisons. J. Geophys. Res.: Oceans, *93*(C5), 4963–4974. doi: 10.1029/JC093iC05p04963

Siedler, G., M. Rouault, A. Biastoch, B. Backeberg, C. J. C. Reason, and J. R. E. Lutjeharms. 2009. Modes of the southern extension of the East Madagascar Current. J. Geophys. Res.: Oceans, *114*, C01005. doi: 10.1029/2008JC004921

Siedler, G., M. Rouault, and J. R. E. Lutjeharms. 2006. Structure and origin of the subtropical South Indian Ocean Countercurrent. Geophys. Res. Lett., *33*, L24609. doi: 10.1029/2006GL027399

Simon, M. H., X. Gong, I. R. Hall, M. Ziegler, S. Barker, G. Knorr, M. T. J. van der Meer, S. Kasper, and S. Schouten. 2015. Salt exchange in the Indian-Atlantic Ocean Gateway since the Last Glacial Maximum: A compensating effect between Agulhas Current changes and salinity variations? Paleoceanography, *30*(10), 1318–1327. doi: 10.1002/2015PA002842

Srokosz, M. A., J. Robinson, H. McGrain, E. E. Popova, and A. Yool. 2015. Could the Madagascar bloom be fertilized by Madagascan iron? J. Geophys. Res.: Oceans, *120*(8), 5790–5803. doi: 10.1002/2015JC011075

SSALTO/DUACS. 2015. SSALTO/DUACS User Handbook: (M)SLA and (M)ADT Near-Real Time and Delayed Time Products. CLS-DOS-NT-06-034. Technical Report 4.4, SALP-MU-P-EA-21065-CLS. Paris: Centre national d'études spatiales.

Svendsen, E., R. Sætre, and M. Mork. 1991. Features of the northern North Sea circulation. Cont. Shelf Res., *11*(5), 493–508. doi: 10.1016/0278-4343(91)90055-B

Swallow, J., M. Fieux, and F. Schott. 1988. The boundary currents east and north of Madagascar: 1. Geostrophic currents and transports. J. Geophys. Res.: Oceans, *93*(C5), 4951–4962. doi: 10.1029/JC093iC05p04951

Ullgren, J. E., E. André, T. Gammelsrød, and A. M. Hoguane. 2016. Observations of strong ocean current events offshore Pemba, northern Mozambique. J. Oper. Oceanogr., *9*(1), 55–66. doi: 10.1080/1755876X.2016.1204172

Ullgren, J. E., H. M. van Aken, H. Ridderinkhof, and W. P. M. de Ruijter. 2012. The hydrography of the Mozambique Channel from six years of continuous temperature, salinity, and velocity observations. Deep Sea Res., Part I, *69*, 36–50. doi: 10.1016/j.dsr.2012.07.003

van der Werf, P. M., P. J. van Leeuwen, H. Ridderinkhof, and W. P. M. de Ruijter. 2010. Comparison between observations and models of the Mozambique Channel transport: Seasonal cycle and eddy frequencies. J. Geophys. Res.: Oceans, *115*, C02002. doi: 10.1029/2009JC005633

Xie, S.-P., H. Annamalai, F. A. Schott, and J. P. McCreary Jr. 2002. Structure and mechanisms of South Indian Ocean climate variability. J. Clim., *15*(8), 864–878. doi: 10.1175/1520-0442(2002)015<0864:SAMOSI>2.0.CO;2

Received: *17 July 2016*; revised: *7 June 2017*.